

Probing local wind and temperature structure using infrasound from Volcan Villarrica (Chile)

J. B. Johnson,¹ J. Anderson,² O. Marcillo,³ and S. Arrowsmith³

Received 2 March 2012; revised 11 July 2012; accepted 16 July 2012; published 6 September 2012.

[1] We use the continuous and intense ($\sim 10^7$ W) infrasound produced by Volcan Villarrica (Chile) to invert for the local dynamic wind and temperature structure of the atmosphere. Infrasound arrays deployed in March 2011 at the summit (2826 m) and on the NNW flank (~ 8 km distant at 825 m) were used to track infrasound propagation times and signal power. We model an atmosphere with vertically varying temperature and horizontal winds and use propagation times (ranging from 23 to 24 s) to invert for horizontal slowness (2.75–2.94 s/km) and average effective sound speeds (328–346 m/s) for NNW propagating infrasound. The corresponding ratio of recorded acoustic power at proximal versus distal arrays was also variable (ranging between 0.15 to 1.5 for the peak 0.33–1 Hz infrasound band). Through application of geometrical ray theory in a uniform gradient atmosphere, these ‘amplification factors’ are modeled by effective sound speed lapse rates ranging from -15 to $+4$ m/s per km. NNW-projected wind speeds ranging from -20 m/s to $+20$ m/s at 2826 m and wind gradients ranging from -11 to $+10$ m/s per km are inferred from the difference between effective sound speed profiles and adiabatic sound speeds derived from local temperature observations. The sense of these winds is in general agreement with regional meteorological observations recorded with radiosondes. We suggest that infrasound probing can provide useful spatially averaged estimates of atmospheric wind structure that has application for both meteorological observation and volcanological plume dispersal modeling.

Citation: Johnson, J. B., J. Anderson, O. Marcillo, and S. Arrowsmith (2012), Probing local wind and temperature structure using infrasound from Volcan Villarrica (Chile), *J. Geophys. Res.*, 117, D17107, doi:10.1029/2012JD017694.

1. Introduction

[2] Seismic energy propagated through the solid earth has long been used to resolve its static internal structure [e.g., *Dziewonski and Woodhouse*, 1987], whereas acoustic probing of the ocean has proven useful for tracking changing velocity structures influenced by changing water temperatures [e.g., *Munk and Forbes*, 1989]. In the atmosphere, structure is both dynamic and anisotropic, and acoustic tomography has been proposed as a potentially powerful imaging tool for quantifying both intrinsic sound speed and winds [*Wilson et al.*, 2001; *Haney*, 2009]. At a regional scale, infrasonic inversion of atmospheric characteristics has been proposed and implemented to resolve wind velocities up to the thermosphere [*Drob et al.*, 2010; *Lalande et al.*, 2012]. Studies by *Le Pichon*

et al. [2005] and *Assink et al.* [2012] have probed the atmosphere using infrasound produced by volcano sources tens to hundreds of kilometers distant.

[3] Local to a volcano infrasound has previously been used to quantify near-source wind and temperature structure [*Fee and Garcés*, 2007; *Matoza et al.*, 2010; *Marcillo and Johnson*, 2010]. These three studies made use of continuous signal from Kilauea’s Halemaumau and Pu’u ‘O’o vents to identify time-dependent signal diffraction and refraction at distances of ~ 12 km [*Fee and Garcés*, 2007; *Matoza et al.*, 2010]. The study by *Marcillo and Johnson* [2010] used relative timing of infrasonic phases recorded across a local network to invert for near-vent winds out to ~ 3 km.

[4] Open vent basaltic volcanoes, such as Kilauea, Ambrym, Villarrica, or Etna, are known for generating intense and continuous infrasound tremor during times when the volcano is not erupting violently [e.g., *Johnson and Ripepe*, 2011]. Such volcanoes are particularly well suited to continuous infrasound probing of the local atmosphere. Volcan Villarrica in Chile, for instance, has been identified an especially ‘loud’ radiator of ~ 1 Hz infrasound during short-duration field campaigns conducted by various groups in 2003, 2004, 2009, and 2010 [*Johnson et al.*, 2004; *Ripepe et al.*, 2010; *Goto and Johnson*, 2011]. These studies recorded infrasound at both the crater rim and on the flanks of

¹Department of Geosciences, Boise State University, Boise, Idaho, USA.

²Department of Earth and Environmental Science, New Mexico Institute of Mining and Technology, Socorro, New Mexico, USA.

³Los Alamos National Laboratory, Los Alamos, New Mexico, USA.

Corresponding author: J. B. Johnson, Department of Geosciences, Boise State University, 1910 University Dr., Boise, ID 83725, USA. (jeffrey.b.johnson@gmail.com)

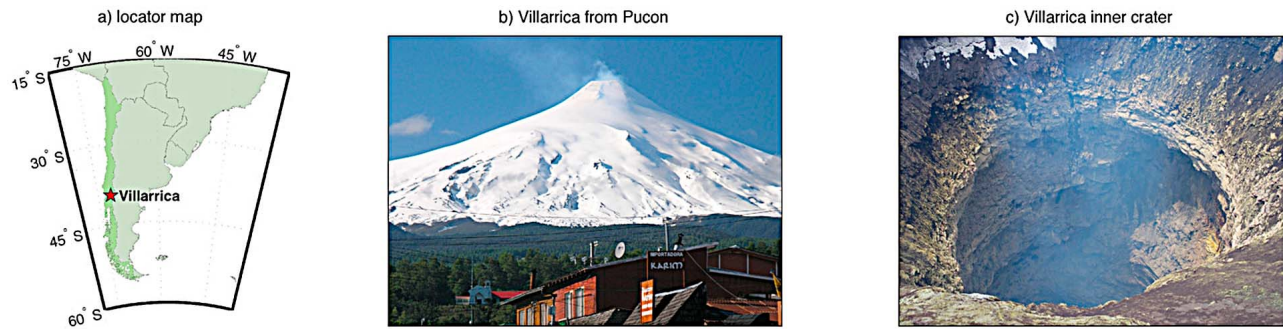


Figure 1. (a) Volcan Villarrica's location within Chile. (b) View of Villarrica 17 km from the city of Pucon. (c) View from crater rim of the ~ 60 -m diameter inner crater. In 2010 lava lake was ~ 60 m below the level of the inner crater rim [Goto and Johnson, 2011].

the volcano out to ~ 4 km. Though the initial motive of these infrasound-grounded projects was to better understand eruption dynamics of the active lava lake, the powerful signal has proven propitious for investigation of atmospheric propagation effects.

[5] During previous Villarrica campaigns intense and continuous infrasonic monotonic, or monochromatic, tremor was identified with peak energy at about 0.7 to 0.8 Hz with amplitudes up to 10^1 Pa (reduced to a distance 1 km). These infrasound levels are sufficiently energetic to have been recorded by regional infrasound array surveillance at a distance of 55 km [Barrientos *et al.*, 2009]. Because Villarrica's summit is accessible for near-source instrument deployment (Figure 1), it is exceptionally well suited for the study of dynamic atmospheric conditions and time-varying propagation effects between the persistent infrasound source and more distant recording sites.

2. Experiment and Data

2.1. Experiment

[6] Toward understanding the atmospheric propagation effects at local distances (defined here as less than a few tens of kilometers), we deployed infrasound arrays near Villarrica's vent and at 8 km to the NNW of the vent (Figure 2) during a week in March of 2011. The summit (SUM) infrasound station comprised a six element linear array of infrasonic microphones spaced at ~ 15 m and extending 75 m radially from the vent (Figure 2e). The closest two microphones were situated within the 150-m diameter summit crater and the estimated slant distance between the ~ 10 -m diameter lava lake vent [Goto and Johnson, 2011] and the nearest array element (SUM1) was ~ 75 m. Stations SUM3, SUM4, and SUM5 were located on a planar bench corresponding to the NNW crater rim at 2826 m above sea level, while SUM6 was located about 10 m downslope on the outside of the summit crater (Figure 2d).

[7] A second infrasound array, referred to as CON array after its proximity to the CONAF (Chilean Forest Service) control station, was situated in dense woods 7740 m to the NNW and 2001 m below the summit station SUM3. The CON array consisted of three elements distributed in an L-shaped topology with ~ 30 m spacing between both CON3 and CON2 and CON1, where the logger was situated (Figure 2f). CON1 and CON2 were positioned equidistant from the

volcano vent and station SUM3, which was at a slant distance of 7910 m.

[8] At both arrays, all sensor elements were connected by cable to a Refraction Technology RT-130 24-bit seismic data logger with GPS timing. Data were acquired continuously at 100 Hz for the duration of the experiment. Both arrays operated coincidentally between Julian day 061 (March 2), 2011 at 13:00 h local time (16:00 UTC) until Julian day 066 (March 7), 2011 at 16:25 h local time. Data were downloaded routinely during daily visits to the summit, but aside from these 5–10 min data gaps, the infrasound records are unbroken throughout the ~ 5 -day period.

[9] Infrasonic signal was recorded with identical broadband microphones utilizing AllSensors™ 0.5-inch (linear to ± 125 Pa) MEMS transducers operated in a differential mode. One side of the pressure sensitive diaphragm was allowed to equilibrate, via 50 micron capillary tubing, to atmospheric pressure at time scales of ~ 100 s. Corner frequencies of these sensors, calibrated with assistance from the Sandia National Labs FACT site, was determined to range from 0.01 to 0.02 Hz [Marcillo *et al.*, 2012], which is at least five octaves below the band of principal Villarrica infrasound. The in-band (< 0.1 Hz to 50 Hz) microphone range is essentially flat and laboratory-calibrated tolerances between sensors are within 1%. Instrument self-noise in the 1–10 Hz band is ~ 2 mPa RMS [Marcillo *et al.*, 2012].

[10] Prior to analytical processing all infrasound data presented in this study were high-pass filtered above 0.125 Hz with a 2-pole Butterworth filter to remove contamination associated with ambient infrasound noise [Bowman *et al.*, 2005]. The higher frequency microbarom 'noise', centered at ~ 0.2 Hz, has some spectral overlap with the Villarrica volcano signal analyzed here, but it is far less intense than the volcano signal recorded at both our array sites.

2.2. Data

[11] Villarrica infrasound recorded in March 2011 is characterized as an intense monotonic (sometimes referred to as 'monochromatic') infrasonic tremor because of its single prominent stable peak at 0.68 Hz (Figure 3). During our study period, the power spectral density was dominated by signal in a narrow 0.33 to 1 Hz band, which contained 81–84% of the total infrasonic power at SUM and 86% of the power at CON. The exceptional similarity of the spectra at these two sites (Figure 3c) suggests that the records were

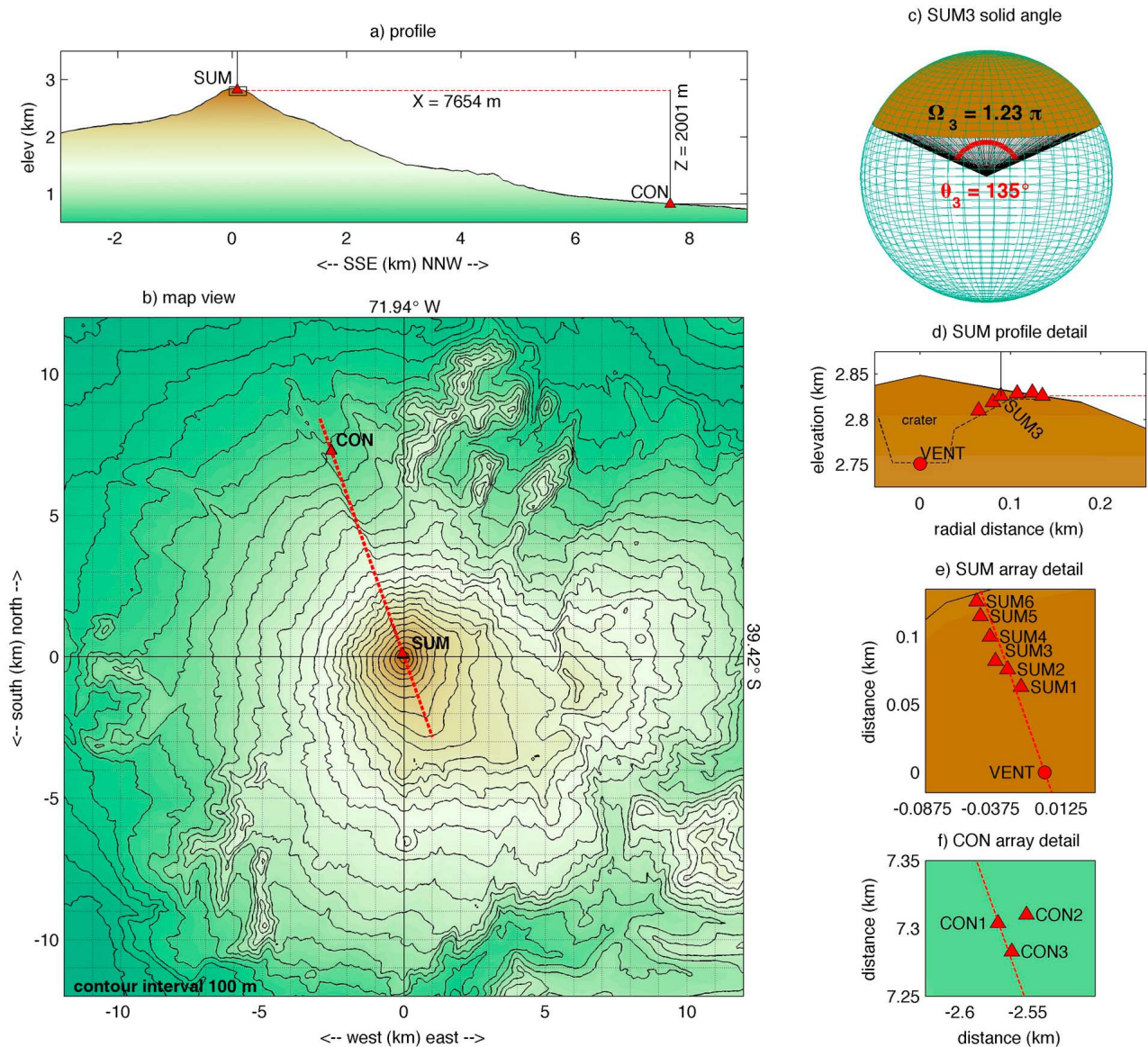


Figure 2. (a) NNW profile illustrating topographic transect between SUM and CON arrays. (b) Map view of Volcan Villarrica showing locations of SUM and CON infrasonic microphone arrays with respect to volcano vent. Profile transect is indicated by dashed red line. (c) Schematic showing inferred apex angles (θ) and solid angles (Ω) for station SUM3 where the solid angle is the area of the spherical surface subtended by the cone. (d) NNW profile detail showing location of summit infrasonic microphones. (e) Plan view detail of SUM linear array. (f) Plan view detail of CON L-shaped array.

dominated by a common source. Although the 0.33 to 1 Hz infrasound overlaps with the microbarom band, which peaks between 0.1 and 0.4 Hz [Bowman *et al.*, 2005], the Villarrica signal was far more intense than the microbarom (~ 18 dB at 0.33 Hz at CON). A microbarom peak is only subtly evident in the CON array spectra (Figure 3c) and contributes negligibly to the total acoustic energy in our band of interest.

[12] During our 5-day observation period the 0.68 Hz frequency peak was remarkably stationary. The peak frequency differed slightly from the stable 0.77 Hz monotone observed a year previously, which had been attributed to Helmholtz resonance for a fixed vent geometry [Goto and Johnson, 2011]. Such Helmholtz resonance has also been

proposed as the mechanism driving infrasound generation at other volcanoes, including Kilauea [Fee *et al.*, 2010]. The lower frequency of the tone recorded in 2011 suggests a modest change in the vent and/or crater geometry.

[13] Waveform detail and spectra show 0.68 Hz sinusoidal oscillations, which are highly coherent across both the arrays and between the different arrays (Figure 4). Structure present in the amplitude-modulated sinusoid allows for determination of precise time lags for microphone records using cross correlation analysis. Similarity between the records from the SUM and CON arrays is exceptional with correlation coefficients generally exceeding 0.97 for 10-min comparison windows (see, for example, Figure 4c). These high correlations

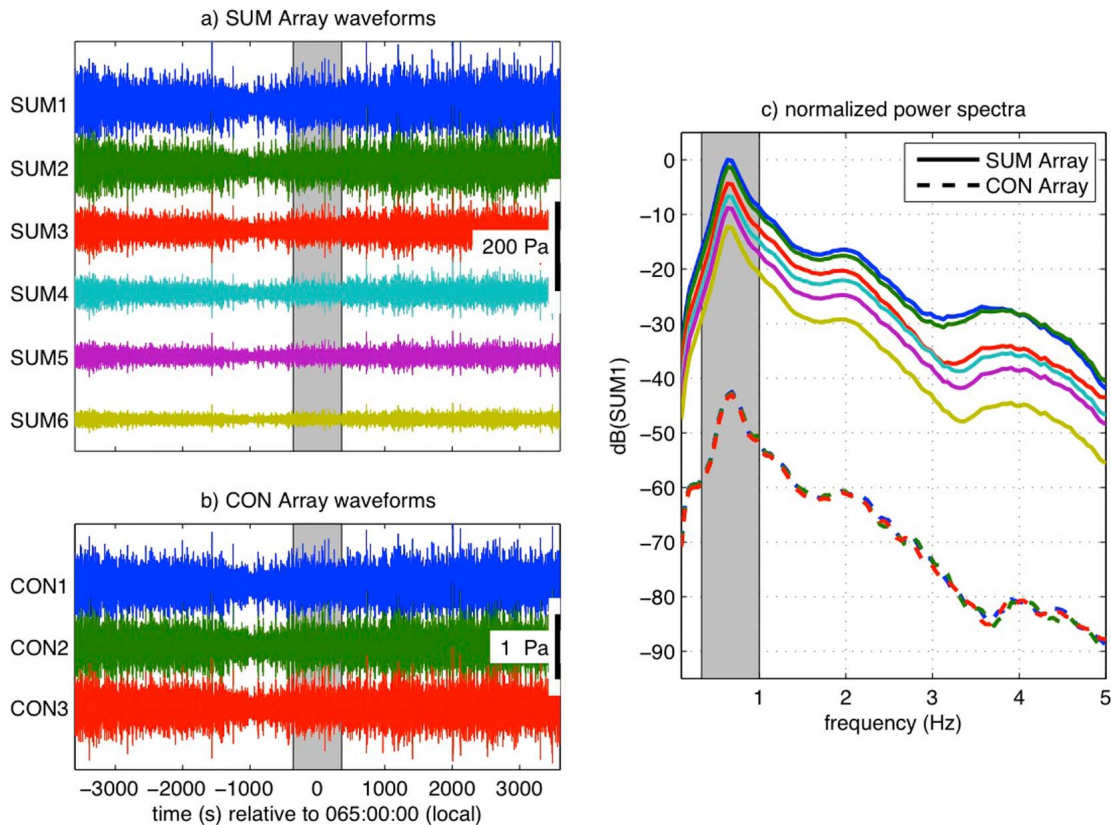


Figure 3. Examples of high passed (>0.125 Hz) 2-h waveforms recorded at (a) the summit and (b) CON ~ 8 km from the vent. Grayed areas indicate waveform detail shown in Figure 4. (c) Corresponding power spectral density is calculated using Welch's averaged periodogram for 20.48 s windows (2048 samples) and normalized relative to peak intensity at SUM1. Gray shading indicates spectral domain used for the power ratio calculations outlined in the text. The microbarom peak, centered at 0.2 Hz [Bowman *et al.*, 2005], is perceptible as a low amplitude shoulder in the CON station power spectra.

substantiate the excellent signal-to-noise ratios at both SUM and CON allowing both lag times and signal intensity ratios to be well quantified.

[14] Propagation times (ΔT) for acoustic waves traveling from the summit to CON are robustly calculated by computing the lag times associated with peak cross-correlation of CON and SUM tremor signals (Figure 5b). In this study SUM3 has been chosen as the near-vent time reference because it is situated close (~ 100 m) to the vent yet its position on the NNW crater rim represents an unimpeded 'line-of-sight' trajectory for sound propagating between SUM3 and CON array. As such, it is the atmospheric structure between sensor nodes SUM3 and CON1 that is probed in this study.

[15] Although peak recorded infrasound amplitudes occasionally exceeded 200 Pa at SUM1, the root mean squared (RMS) infrasound signal amplitude averaged 24.6 Pa at the nearest SUM array element (SUM1; ~ 75 m from the vent) and fell to 6.9 Pa at the furthest SUM array element (SUM6; ~ 145 m from the vent) (Figure 5c). Such fall-off in RMS pressure amplitudes for the SUM array elements is more severe than would be predicted for a simple inverse-distance geometric pressure decrease. The excess fall-off is partially explained by the increasing solid angle of the atmosphere moving from the interior of the funnel-shaped summit crater (SUM1–2) to the crater lip (SUM3–5) and beyond (SUM6).

[16] To first order, the relative solid angles at the various SUM array elements can be estimated by assuming an isotropic vent source with dynamic acoustic energy that is conserved for fractional spherical shells varying with radial distance (r) [Vavryčuk, 1994]. We hold this radially directed far-field energy constant and calculate solid angles (Ω) for each of the SUM microphones that will conserve the total dynamic energy, a product of RMS recorded excess pressure and cross-sectional area [e.g., Dowling, 1998]. Supposing that the solid angle for SUM5 is 2π (appropriate for a hemispherical space) then solid angles for SUM1–6 would respectively be 0.92π , 0.80π , 1.23π , 1.86π , 2.00π , and 3.12π using the time-averaged RMS pressures from Figure 5c.

[17] These solid angles correspond to subtending cones with apex angles (θ) of 114° , 106° , 135° , 172° , 180° , and $\sim 248^\circ$, where $\theta = 2 \cos^{-1}(1 - \Omega/2\pi)$ (refer to Figure 2c for schematic of solid angle and apex angle). In general, the apex angles are in decent agreement with the flaring shape of the crater and rim of Villarrica and suggest minimal diffraction effects in this low frequency band. We propose that the topography of the Villarrica summit crater (~ 150 m diameter and ~ 100 m deep) exerts a negligible influence on the long wavelength (1 km to $1/3$ km) infrasound that is investigated here.

[18] Compared to the 24.6 Pa RMS pressure amplitude at SUM1, the three elements of the CON array (at a vent distance

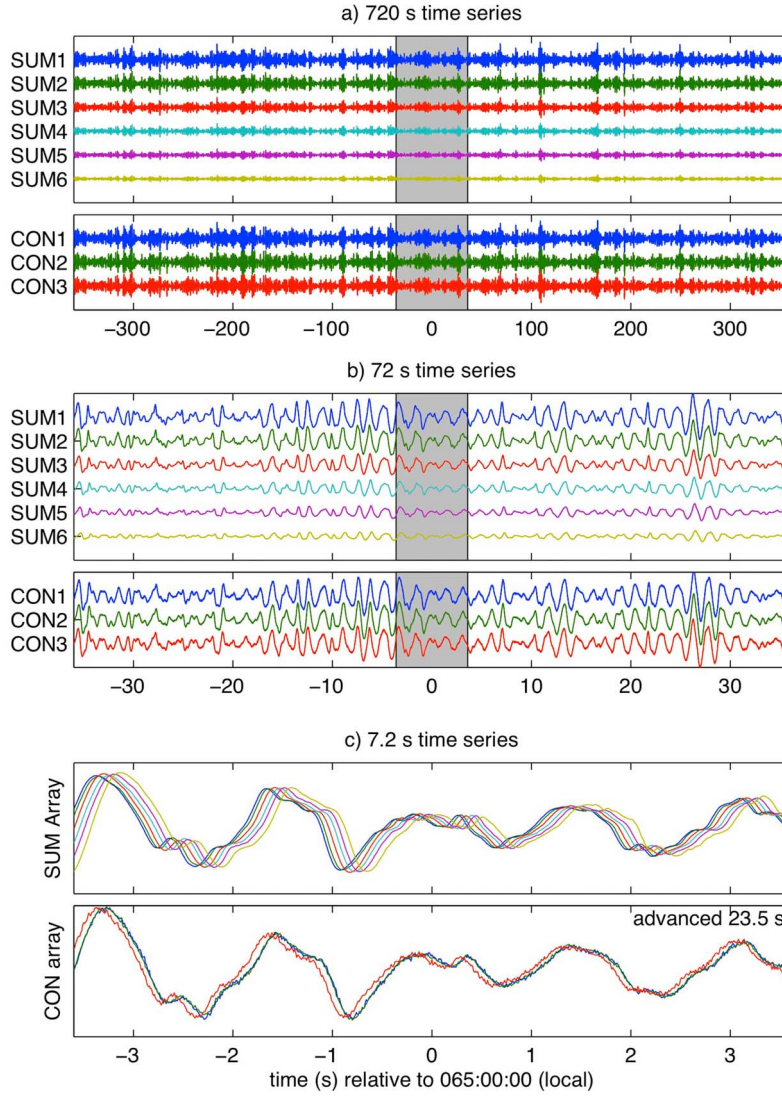


Figure 4. Detail of waveforms recorded at SUM and CON filtered above 0.125 Hz. Relative to the waveforms shown in Figure 3 the detail shows time axes with (a) $10\times$ time magnification, (b) $100\times$ magnification, and (c) $1000\times$ magnification. CON waveforms have been advanced by 23.5 s to account for typical propagation time between SUM3 and CON1.

of ~ 8000 m) recorded RMS amplitudes of 0.21 Pa (after filtering above 0.125 Hz to reduce ambient noise; Figure 5c). The mean pressure amplitude ratio between the SUM1 signals and the CON array signals was 117 while the source-receiver distance ratio of these respective stations was 107. Considering that far-field power density is proportional to the square of the pressure amplitudes and inversely proportional to the atmospheric impedance ($c\rho$) we estimate the ~ 5 day cumulative energy density at station j using

$$w_j = \int_{J_{day61}}^{J_{day66}} \frac{p_j^2}{c_j \rho_j} dt \quad (1)$$

where acoustic radiation is assumed to propagate radially outward.

[19] For $p_{rms} = 24.6$ Pa (at SUM1), $c_{SUM1} = 343$ m/s, and $\rho_{SUM1} = 0.75$ kg/m³ (~ 3000 m altitude) equation (1) gives a

cumulative energy density of 1.05×10^6 J/m² at the summit. For $p_{rms} = 0.21$ Pa (at CON), $c_{CON} = 343$ m/s, and $\rho_{CON} = 1.00$ kg/m³ the energy density at the CON array is 76 J/m². Assuming that total acoustic energy is conserved and is constant over a fractional spherical shell then the ratio of SUM1 and CON solid angles must be $\frac{\Omega_{CON}}{\Omega_{SUM1}} = \frac{r_{SUM1}^2}{r_{CON}^2} \frac{w_{SUM1}}{w_{CON}} = 2.1$.

Supposing, from topographic profiles, that Ω_{SUM1} is $\sim 0.9 \times \pi$ at 75 m (i.e., $W_{SUM1} = 2.8 \times 10^{10}$ J) then Ω_{CON} would be $1.9 \times \pi$, which would give an apex angle of 174° . This estimated value is approximately a half-space and is similar to the apex angle of 209° estimated from topography.

[20] The solid angle ratio of 2.1 determined above assumes sound radiated into a non-moving and homogeneous atmosphere, which is clearly an idealization. In reality, sound radiation in a structured atmosphere results in potential intensification for certain directions and distances and

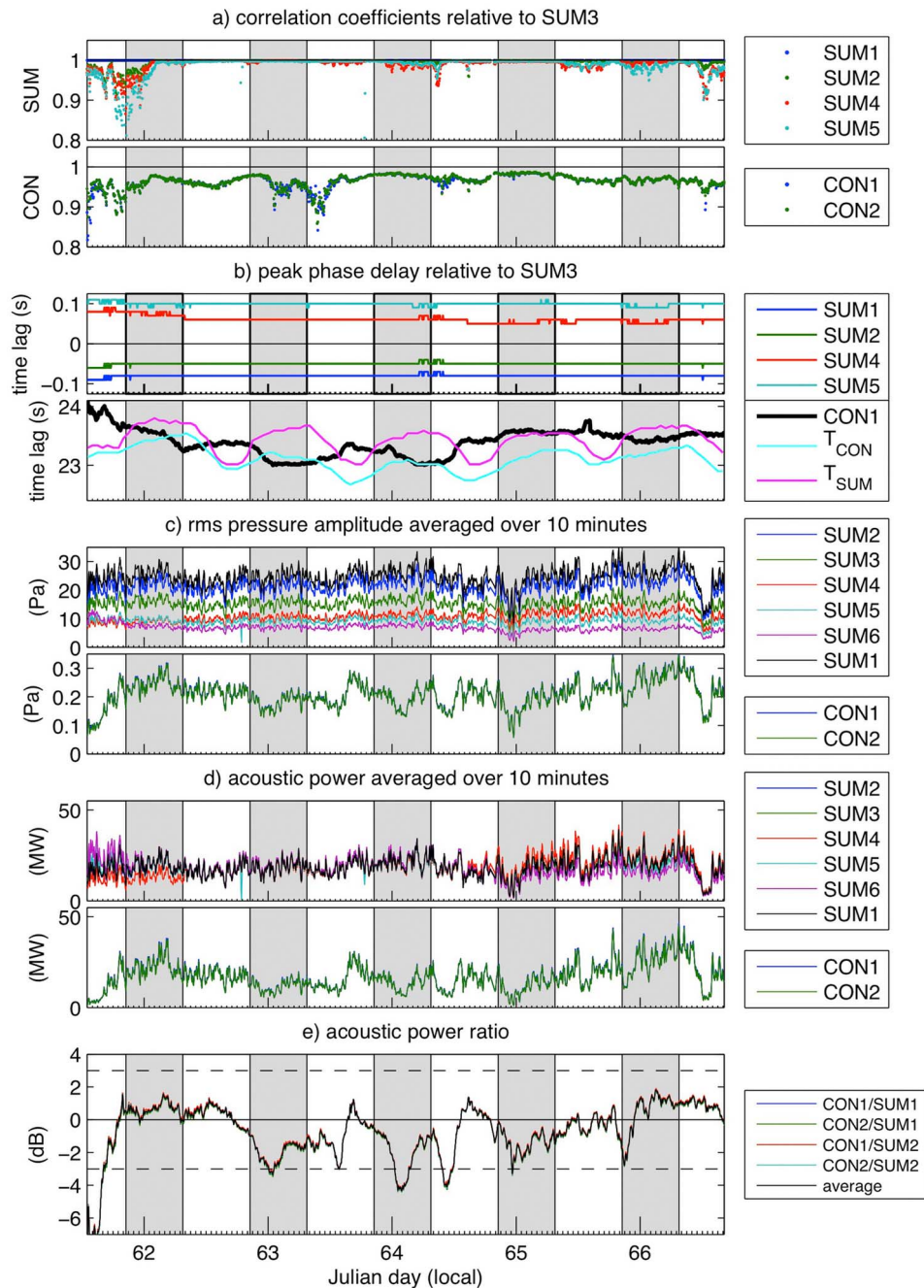


Figure 5. (a) Normalized cross-correlation coefficients between SUM3 and other SUM and CON array elements shown for 10-min signal windows filtered above 0.125 Hz. Generally, cross-correlation values are above 0.95 except when wind noise contributes incoherent noise to one or more array elements. (b) Phase lags are shown for the peak cross correlation values shown in Figure 5a. For data from the CON array these propagation times are compared with predicted propagation times using temperature records from SUM and CON and assuming a non-moving atmosphere. (c) Ten-minute RMS infrasound amplitudes are shown for 6 array elements from SUM and 2 array elements from CON. (d) Band-limited (0.33 to 1 Hz) infrasound power is shown for 6 array elements from SUM and 2 array elements from CON. (e) Ratios of CON / SUM band-limited infrasound power are shown in dB relative to the power ratio expected for a uniform atmosphere. All data are shown for 10-min windows with 5-min overlap. Grayed areas indicate local nighttime.

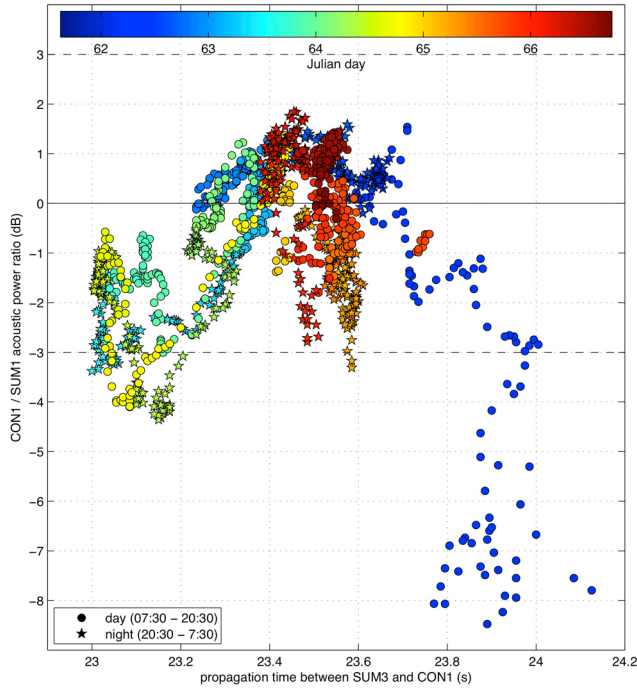


Figure 6. Evolution of propagation times versus amplification effects for ~ 5 days of monitoring at Volcan Villarica. The 1453 points correspond to correlated time lags and power ratios for successive ten minute time windows with five minute overlap. The 0 dB solid line corresponds to an expected power ratio for a homogeneous non-moving atmosphere. Dashed lines indicate ± 3 dB power ratios, relative to a non-moving atmosphere.

diminution of sound energy density elsewhere. In order to quantify this ‘amplification effect’, and its evolution over time, we calculate the sound energy recorded at CON and SUM by assuming (from topography) solid angles of $2.5 \times \pi$ at CON and $0.9 \times \pi$ at SUM1. We also assume that the summit region acts as a spherical radiator of sound into a fractional wholospace with the specified solid angles.

[21] To quantify time-averaged power at a specific station we analyze 10 min data intervals with 5 min overlap. For a time window starting at sample t_0 and with duration $\tau = 60,000$ samples (10 min) we identify array-specific signal windows, which account for acoustic retardation times (r_j/c), i.e., $t_j > t_0 + r_j/c$ and $t_j < t_0 + r_j/c + \tau$. A discrete Fourier transform $p(\omega)$ is then calculated for this sample window as

$$p_j(\omega) = \sum_{t=t_0+r_j/c}^{t_0+r_j/c+\tau} p_j(t) \cdot e^{-i2\pi\omega t/\tau} \quad (2)$$

We then quantify the power for band-limited (between ω_l and ω_h) infrasound by integrating spectral density in the frequency domain as

$$P_j(t, \omega) = \frac{\Omega_j r_j^2}{c \rho_j} \int_{\omega_l}^{\omega_h} \frac{|p_j(\omega)|^2}{\tau} d\omega \quad (3)$$

In this study power is calculated for frequencies between 0.33 and 1 Hz (~ 2.1 to 6.2 radians s^{-1}). Solid angles and

atmospheric properties are station-specific and fixed at the values previously specified. Band-limited power for elements of the SUM and CON arrays are displayed in Figure 5d. The evolving ratio of powers of CON relative to SUM1 is indicated by $P_R(t) = P_{CON}/P_{SUM}$ and can be displayed in terms of decibels as $10 \times \log_{10}(P_R)$ (Figure 5e). Together with the propagation times (ΔT) in the bottom panel of 5b these amplification effects (P_R) are used to characterize evolving atmospheric conditions between SUM and CON for overlapping ten-minute time intervals (Figure 6).

3. Analysis

[22] To invert for atmospheric properties we solve for a simplified atmospheric structure entailed by the following three conditions: 1) atmospheric parameters vary only as a function of altitude, 2) winds are confined to horizontal planes, and 3) the effective sound speed possesses a uniform vertical gradient. The first two assumptions are commonly invoked in atmospheric modeling and the third assumption implies that both temperature and wind profiles independently have linear gradients between altitudes of about 1 and 3 km. This is an approximation, which is often reasonable for the lowermost troposphere above an atmospheric boundary layer that is typically hundreds of meters to a couple kilometers in height [Stull, 2000]. A discussion of this last assumption and its implications for our modeling is given in section 4.0.

[23] Given the above assumptions ΔT and P_R can uniquely constrain both the average effective sound speed and its lapse rate. Effective sound speed is a combination of adiabatic sound speed (v) and the horizontal wind velocity (u) projected in the direction of the acoustic flight path, $c(z) = v(z) + \vec{u}(z) \cdot \vec{r}$ [e.g., Garcés *et al.*, 1998]. In this study we solve for an effective sound speed that is a function of a constant lapse rate α defined by $c(z) = c_{CON} + \alpha z$, where c_{CON} is the effective sound speed at 825 m at the altitude of station CON.

[24] Although a constant gradient lower troposphere is clearly a simplification of the real atmosphere it allows us to solve for a linear atmospheric profile, which replicates the gross-scale structure of the medium. In section 3.1 we indicate how ΔT is largely controlled by the average effective sound speed (or horizontal slowness) while in section 3.2 we demonstrate how P_R is primarily controlled by effective sound speed lapse rate, which focuses or defocuses acoustic rays. Following constraints upon the adiabatic sound speed using meteorological temperature input, we are then able to separate out the advection contributions (i.e., wind) to the effective sound speed in section 3.3.

[25] Comparison of these inversion results with radiosonde observations are given in section 4.0. Radiosonde data from weather balloons launched from the Puerto Montt airport (~ 230 km from Volcan Villarica) illustrate lower atmospheric structure in the region during our period of study (Figure 7).

3.1. Horizontal Slowness and Effective Sound Speed Profiles

[26] In a non-advecting homogeneous fluid with constant adiabatic sound speed elastic waves will propagate to a

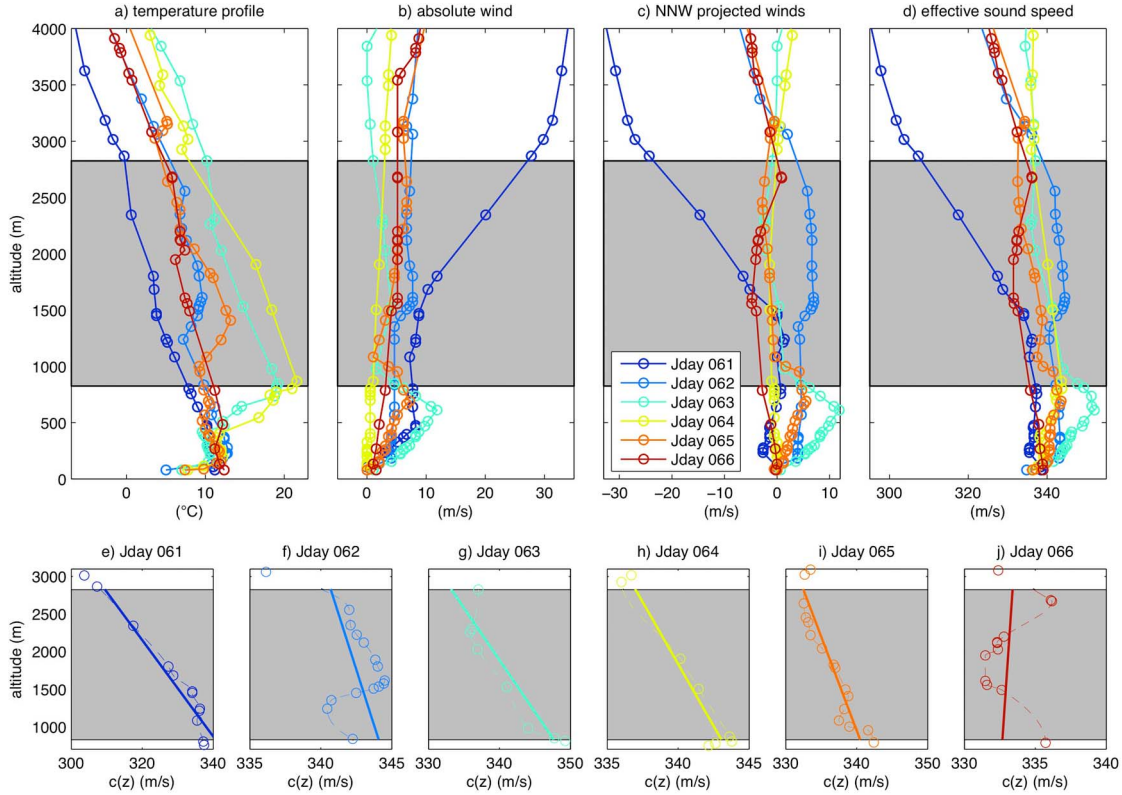


Figure 7. (a) Temperature profiles from daily Puerto Montt airport radiosondes launched at 9 A.M. local time on March 2 (Julian day 061) through March 7 (Julian day 066). (b) Radiosonde-measured absolute wind speeds. (c) NNW projected wind speeds. (d) Effective sound speed profiles calculated from data in Figures 7a and 7c for NNW-directed sound propagation (refer to section 3.3). (e–j) Detail of daily effective sound speed profiles, fit by cubic interpolation, between 700 m and 3100 m altitude. Straight line segments are linear regressions of the original data shown with open circles. Grayed areas in all panels correspond to the altitude range probed in this study.

horizontal distance X and vertical distance Z with a constant angle relative to the vertical, i.e., $i = \tan^{-1}(X/Z)$. This take-off, or incidence angle, is related to the ray parameter, or horizontal slowness s_x , by $i = \sin^{-1}(s_x c)$. Horizontal slowness can be written in terms of X and Z where $c = (\sqrt{X^2 + Z^2})/\Delta T$:

$$s_x = \frac{X \Delta T}{X^2 + Z^2} \quad (4)$$

In a vertically graded atmosphere with constant sound speed lapse rate α acoustic waves will refract according to ray theory and trace an arc of a circle. Throughout the raypath trajectory the ray parameter remains constant and is defined by $s_x = \sin i(z)/c(z)$. For a non-turning (uniformly down-going) ray in a constant gradient atmosphere the horizontal distance traveled may be determined analytically [Slotnick, 1959] as a function of vertical distance by

$$x(z) = \frac{\sqrt{1 - s_x^2 c(z)^2} - \sqrt{1 - s_x^2 c_0^2}}{\alpha s_x} \quad (5)$$

where c_0 is the effective sound speed at the ray end point. The travel time over the same vertical distance z is [Slotnick, 1959]

$$t(z) = \frac{1}{\alpha} \ln \left[\frac{c_0}{c(z)} \frac{\left(1 + \sqrt{1 - s_x^2 c(z)^2}\right)}{\left(1 + \sqrt{1 - s_x^2 c_0^2}\right)} \right] \quad (6)$$

For our geometry at Volcan Villarrica the total vertical distance descended is the elevation drop between SUM3 and CON1, which is $Z = 2001$ m. From equation (5) the corresponding horizontal distance traversed is

$$X(s_x, c_{CON}, c_{SUM}) = \frac{Z}{c_{SUM} - c_{CON}} \frac{\left[\sqrt{1 - s_x^2 c_{CON}^2} - \sqrt{1 - s_x^2 c_{SUM}^2} \right]}{s_x} \quad (7)$$

where c_{SUM} is the effective sound speed at SUM3 (substituted for c_0 in equation (5)) and c_{CON} is the sound speed at the

distant receiver. For the geometry at Villarrica the horizontal distance between SUM3 and CON1 is fixed at $X = 7654$ m. Propagation time from equation (6) becomes

$$\Delta T(s_x, c_{CON}, c_{SUM}) = \frac{Z}{c_{SUM} - c_{CON}} \ln \left[\frac{c_{SUM} \left(1 + \sqrt{1 - s_x^2 c_{CON}^2} \right)}{c_{CON} \left(1 + \sqrt{1 - s_x^2 c_{SUM}^2} \right)} \right] \quad (8)$$

In these equations, velocity lapse rate α has been substituted with c_{CON} , c_{SUM} and Z .

[27] For a range of potential slowness values and propagation time data we numerically calculate the values of bounding sound speeds that satisfy both equations (7) and (8). We perform a grid search for all possible values of c_{CON} and c_{SUM} to minimize the sum of the squared fractional errors in X and ΔT :

$$R = \left(1 - \frac{1}{X} \frac{Z}{c_{SUM} - c_{CON}} \frac{\left[\sqrt{1 - s_x^2 c_{CON}^2} - \sqrt{1 - s_x^2 c_{SUM}^2} \right]}{s_x} \right)^2 + \left(1 - \frac{1}{\Delta T} \frac{Z}{c_{SUM} - c_{CON}} \ln \left[\frac{c_{SUM} \left(1 + \sqrt{1 - s_x^2 c_{CON}^2} \right)}{c_{CON} \left(1 + \sqrt{1 - s_x^2 c_{SUM}^2} \right)} \right] \right)^2 \quad (9)$$

[28] Minimum residual solutions indicate that a range of takeoff angles, (linear) atmospheric profiles, and unique raypaths can give a single propagation time (gray lines and symbols in Figures 8a and 8c). Notably, both downward refracting and upward refracting rays can result in the same travel time. Constraining the precise travel raypath, and corresponding upper and lower sound speeds, requires additional information about the degree of acoustic focusing.

3.2. Infrasound Focusing and Its Dependence on Atmospheric Structure

[29] In a homogeneous non-attenuating atmosphere acoustic far-field intensity falls off with the inverse squared distance from a compact volumetric source. For the propagation distance of ~ 8 km presented in this study intrinsic attenuation is negligible at low frequencies of less than 1 Hz [e.g., *Bass and Bauer*, 1972]. As such, deviation from idealized $1/r^2$ energy fall-off is attributable to topographic, or site effects, as well as to non-uniform atmospheric structure. Here we consider that recording site effects are negligible, or at least constant, and that topographic obstructions are minimal except for perhaps the most extreme upward refracting raypaths (Figures 8a and 8b). Variations in observed power ratios are thus primarily due to variable ray focusing caused by changing atmospheric structure.

[30] We use elastic wave ray theory to predict the intensity of acoustic signals for varying atmospheric structures. For a vertically stratified medium *Lay and Wallace* [1995] provide an analytical expression for acoustic energy density as a function of takeoff angle i_z , propagation time ΔT , and horizontal distance propagated X :

$$E(X) \propto c(z) \left(\frac{\tan i(z)}{X \cos i(z)} \right) \left(\frac{d^2 \Delta T}{dX^2} \right) \quad (10)$$

Rewriting in terms of ray parameter, where $s_x = d\Delta T/dX$, this equation becomes

$$E(X) \propto \left(\frac{s_x c(z)^2}{X (1 - s_x^2 c(z)^2)} \right) \left(\frac{ds_x}{dX} \right) \quad (11)$$

The change of distance with ray parameter can be found by differentiating equation (7) with respect to s_x , yielding

$$\frac{dX}{ds_x} = Z \frac{\epsilon_{SUM}^2 \epsilon_{CON} - \epsilon_{CON}^2 \epsilon_{SUM} + (s_x^2 c_{SUM}^2) \epsilon_{CON} - (s_x^2 c_{CON}^2) \epsilon_{SUM}}{(c_{SUM} - c_{CON}) s_x^2 \epsilon_{CON} \epsilon_{SUM}} \quad (12)$$

where the substitution $\epsilon(z) = \sqrt{1 - s_x^2 c(z)^2}$ has been introduced.

[31] Energy as a function of distance for a vertically varying medium then becomes

$$E(X) \propto \frac{s_x c_{SUM}^2}{X Z (1 - s_x^2 c_{SUM}^2)} \times \frac{(c_{SUM} - c_{CON}) s_x^2 \epsilon_{CON} \epsilon_{SUM}}{\epsilon_{SUM}^2 \epsilon_{CON} - \epsilon_{CON}^2 \epsilon_{SUM} + (s_x^2 c_{SUM}^2) \epsilon_{CON} - (s_x^2 c_{CON}^2) \epsilon_{SUM}} \quad (13)$$

This can be compared with energy density for a homogeneous, non-moving medium (i.e., where $dc(z)/dz = 0$) where energy density falls off with the inverse of distance squared:

$$E_H(X) \propto \left(\frac{1}{X^2 + Z^2} \right) \quad (14)$$

[32] The predicted power (or energy) ratio is then

$$P_R(X) = \frac{E}{E_H} = \frac{X^2 + Z^2}{X Z} \frac{\epsilon_{CON}}{\epsilon_{SUM}} \frac{c_{SUM}^2 (c_{SUM} - c_{CON}) s_x^3}{\epsilon_{SUM}^2 \epsilon_{CON} - \epsilon_{CON}^2 \epsilon_{SUM} + (s_x^2 c_{SUM}^2) \epsilon_{CON} - (s_x^2 c_{CON}^2) \epsilon_{SUM}} \quad (15)$$

Using travel times ΔT and power ratios P_R from recorded data both the ray parameter as well as sound speed gradients can be numerically determined by minimizing equation (9) and then plugging the potential solutions for c_{SUM} , c_{CON} , and s_x into equation (15). For a specified travel time between SUM and CON and a value of P_R the upper and lower effective sound speeds are uniquely determined (e.g., Figure 8c).

[33] Though our solutions are modeled for raypaths propagating unobstructed through the atmosphere we note that certain raypaths depicted in Figures 8a and 8b appear to graze local topography. Those rays correspond to modeled power ratios of less than -6 dB, which are observed during a brief period on Julian day 061. We consider that during this exceptional period some additional sound diminution could be due to diffraction caused by the intervening topography. For the most part relatively unimpeded transmission is likely, especially given the long wavelengths ($>1/3$ km) of the primary infrasound (<1 Hz) energy.

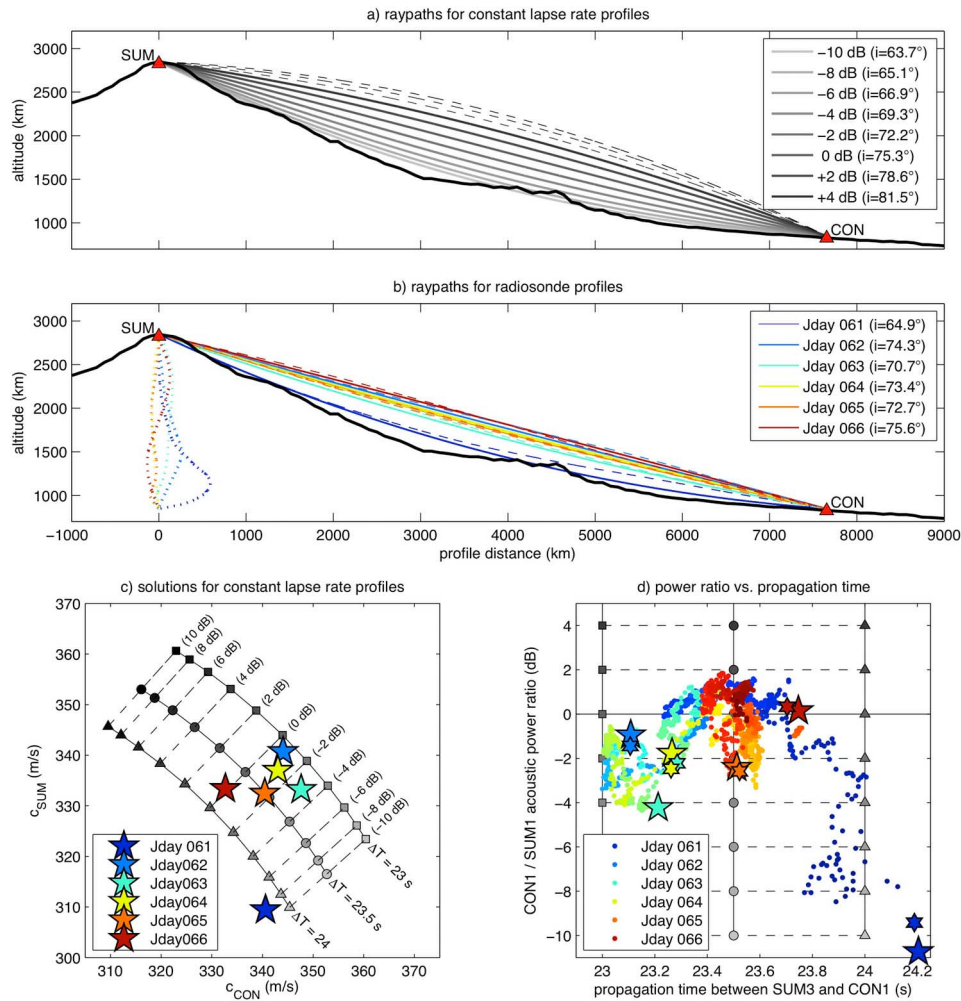


Figure 8. (a) Raypaths shown for a variety of lapse rates that deliver a range of acoustic energy focusing values from -10 dB to $+4$ dB (solid lines) relative to a homogeneous atmosphere and calculated according to equation (15). Dashed lines corresponding to downward refractions with $+6$, $+8$, and $+10$ dB energy ratios that are not observed in our data. (b) Raypaths shown for atmospheric structure corresponding to radiosonde profiles from Figure 7. Solid lines are raypaths calculated for constant lapse rate (linear regression of profiles in Figures 7e–7j). Dashed lines are raypaths for cubic interpolation of profiles (dashed lines in Figures 7e–7j). Dotted line profiles show the horizontal difference between the two raypath trajectories. (c) Combinations of lower and upper effective sound speed bounds for constant lapse rate profiles that satisfy propagation times according to equation (9). Colored pentagrams correspond to constant lapse rate atmospheres and solid line raypaths in Figure 8b. (d) Power ratios versus propagation times predicted for various raypaths. Gray scale symbols correspond to those in Figures 8a and 8c. Colored pentagrams correspond to linear gradients (solid lines) from radiosonde data in Figure 8b. Smaller colored hexagrams correspond to dashed-line raypaths in Figure 8b. Background scatterplot shows power ratios and propagation times recorded by the SUM and CON arrays for the entire study period and is the same as Figure 6. Color convention for Julian day data is consistent in Figures 6, 7, and 8.

3.3. Conversion of Effective Sound Speed Profiles to Temperature and Wind Structure

[34] Under the assumption of a constant lapse rate, effective sound speed is related to altitude by $c(z) = (c_{SUM} - c_{CON})(z/Z) + c_{CON} = \alpha z + c_{CON}$ where z is relative to the 825 m elevation of CON. The lapse rate convention used here is negative for effective sound speed that decreases with altitude, such as generally occur in a normally stratified atmosphere. In general effective sound speeds are greater for

higher temperatures and for winds that favorably drive the acoustic signal from the source toward the distant array. In our inversion the profiles of effective sound speed are calculated as they vary with time (Figure 9a).

[35] Effective sound speed is considered here as a linear sum of adiabatic sound speed $v(z)$, which is a function of air temperature, and wind, which contributes to advection of sound along a raypath. This advection presumes horizontal winds that are projected onto the acoustic flight direction, i.e., $\vec{u}(z) \cdot \vec{r}(z)$. Projected horizontal winds can then be calculated

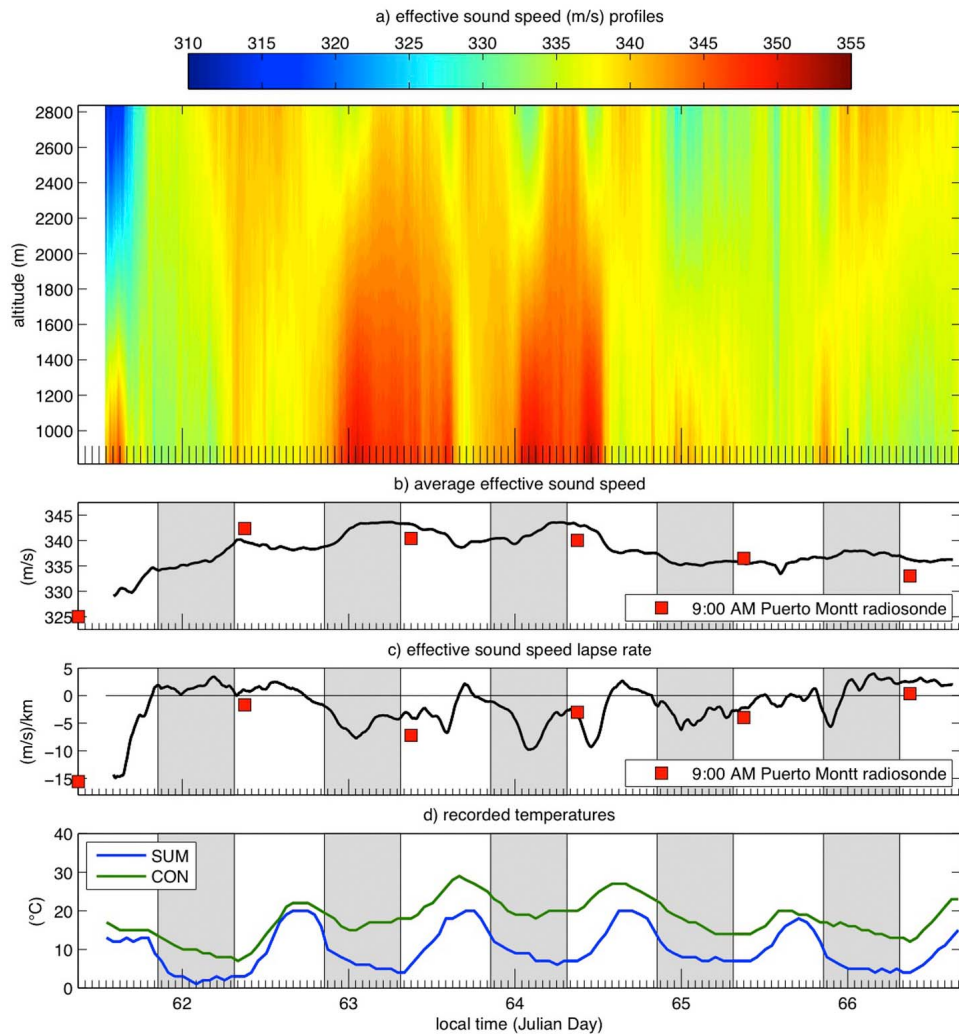


Figure 9. (a) \sim 5-day summary of variations in effective sound speed profiles calculated at 10 min intervals with 5 min overlaps. Records of (b) profile-averaged effective sound speeds and (c) effective sound speed gradients (or lapse rates). In both Figures 9b and 9c the square symbols indicate average effective sound speed and effective sound speed lapse rate calculated for NNW projections of the radiosonde data (refer to Figure 7 profiles). (d) Corresponding temperature data taken from the digitizers' internal sensors and sampled hourly. Grayed areas indicate local nighttime.

from effective sound speed profiles and knowledge of the adiabatic temperature gradient:

$$\bar{u}(z) \cdot r(z) = c(z) - v(z) \quad (16)$$

The adiabatic sound speed is calculable for known atmospheric temperature profiles, i.e., $v(z) = \sqrt{\gamma RT(z)} = \sqrt{402.8 \times T(z)}$, where γ is the ratio of specific heats, R is the ideal gas constant, and T is the temperature of the air in kelvins. In order to extract time-evolving wind profiles, we convert temperature observations at CON and SUM to adiabatic sound speeds, and then apply a linear adiabatic sound speed gradient. For a range of reasonable temperatures (e.g., 0–25°C) the adiabatic sound speed variation with temperature (i.e., dv/dT) is nearly linear.

[36] We incorporate temperature data that were recorded hourly with thermometers embedded in the RT-130 data

loggers at both CON and SUM and assume a near-linear temperature gradient between these elevations. The data logger temperature records show realistic values, with lower altitude stations showing systematically warmer temperatures, and both stations showing clear diurnal fluctuations (Figure 9d). Though we utilize these temperature records to infer bounding adiabatic sound speeds for our study medium we acknowledge several potential limitations of these data. Most notably we have neglected boundary layer temperature considerations and potential localized solar heating of the data loggers, which may artificially elevate the RT-130 thermal sensor. We tried to minimize solar heating effects by locating station CON in forested areas and isolating SUM from the sun beneath a rock pile.

[37] Altitude-varying horizontal winds projected to the NNW are found as the difference between inferred effective sound speeds and modeled adiabatic sound speeds (equation (16); Figure 10d). With the exception of Julian

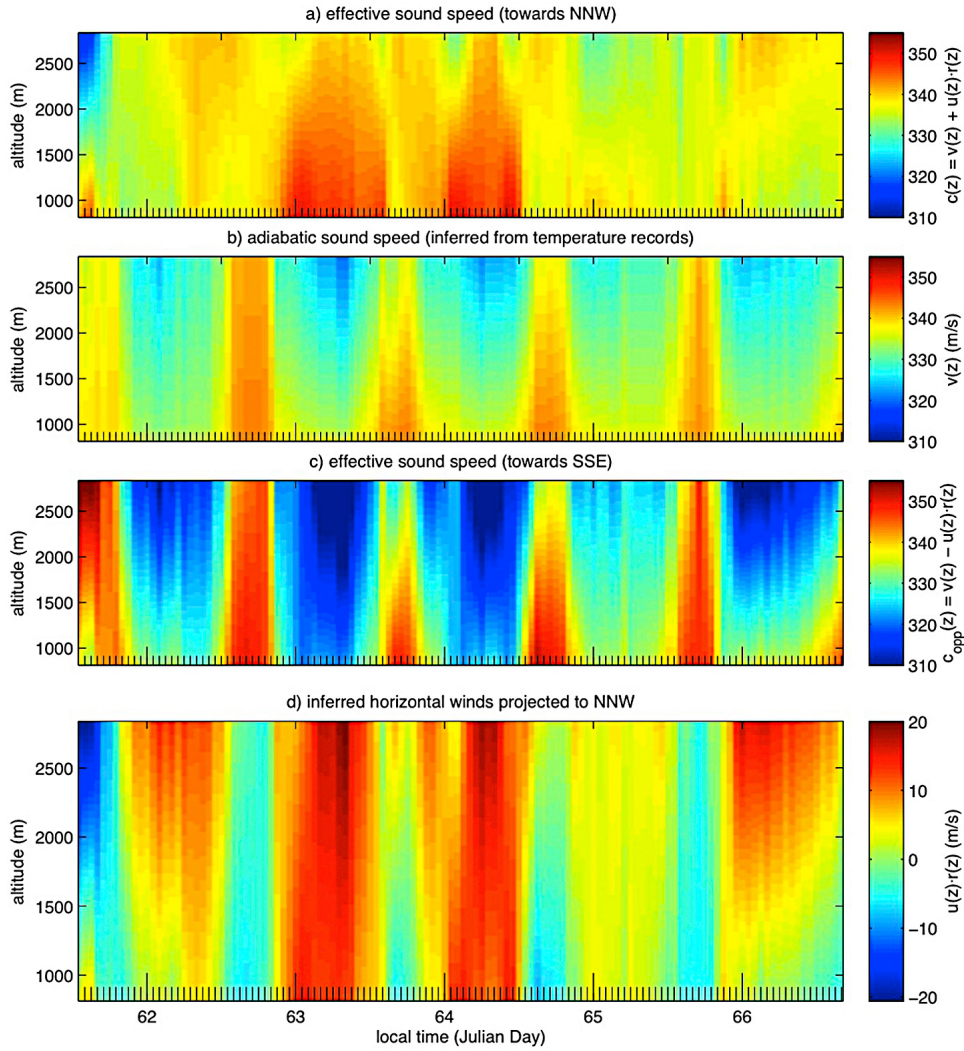


Figure 10. (a) Hourly averaged effective sound speed profiles (toward NNW) derived from propagation time and acoustic power ratio data. (b) Hourly adiabatic sound speed profiles derived from CON and SUM temperature data assuming a linear sound speed gradient between these stations. (c) Effective sound speed to the SSE inferred from effective sound speed to the NNW and adiabatic temperature profiles calculated according to equation (17). (d) Inferred horizontal winds projected to the NNW according to equation (16).

day 061, the inferred winds appear to be positive when projected to the NNW and generally indicate a positive shear with increasing altitude. Although the precise direction of the winds are not constrained in these 1-D profiles, we can estimate the effective sound speed in the opposite direction (to the SSE) by assuming that winds are uniform on both sides of the volcano (Figure 10c). In this case the projection unit vector is opposite to the NNW trajectory and effective sound speed toward the SSE becomes

$$c_{opp}(z) = 2 \times v(z) - c(z) = v(z) - u(z) \cdot r(z) \quad (17)$$

4. Results and Comparison of 2-D Wind Inversion With Radiosonde Data

[38] During our 5-day study interval, strong diurnal temperature fluctuations, which control adiabatic sound speeds,

did not directly correlate with infrasound-derived effective sound speeds (compare for example the shape of the curves in Figures 9b and 9d). This poor correlation suggests there is a substantial influence from time-variable winds, which can either increase (e.g., on Julian day 061) or diminish (e.g., during late night through mornings on Julian days 062 through 066) the infrasound propagation times (see Figure 10d). Considering that temperatures are relatively low during both night and early morning our data indicate a predominance of early morning high-altitude Southerlies, which serve to advance sound toward CON. After Julian day 061 our modeled wind profiles indicate a diurnal behavior, which compares favorably to the average seasonal meteorological trends recorded locally at weather station IARAUCAN3 situated 15 km to the North of Volcan Villarrica. Although IARAUCAN3 was not operational in March of 2011 records from March 2012 typically reveal increased intensity winds during mid-day.

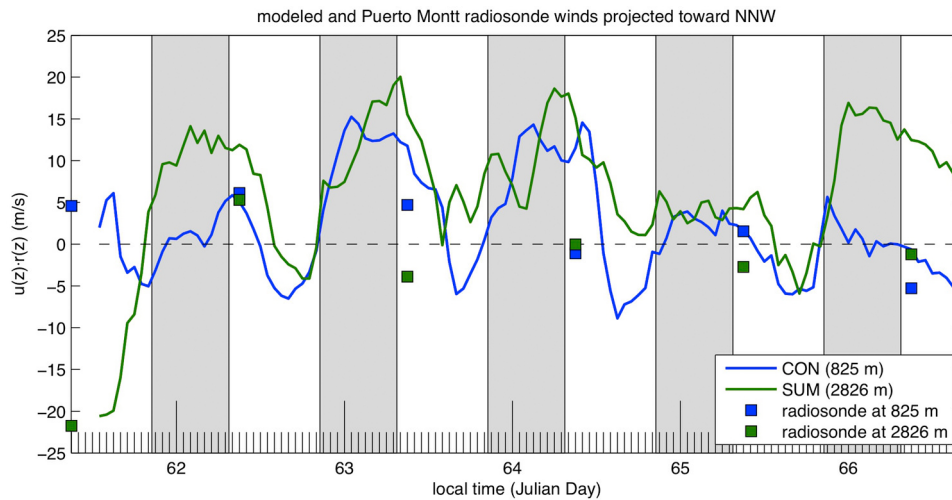


Figure 11. Hourly infrasound-derived winds at 2826 m (altitude of SUM) and 825 m (altitude of CON) compared with wind observations (square symbols) from the Puerto Montt radiosonde taken daily at 9:00 A.M. local Chilean time. Radiosonde winds at altitudes of SUM and CON are calculated using a linear regression of all data points between 700 and 3100 m. Grayed areas indicate local nighttime.

[39] Our NNW polarized wind inversion profiles correspond to localized structure for which the sound rays propagate only between SUM and CON. Nonetheless it is illuminating to compare these results with wind data available from regional radiosonde observations. In March 2011 daily radiosondes were launched 230 km from Villarrica at 9:00 A.M. local time. For the radiosonde-derived parameters shown in Figures 9b and 9c effective sound speeds and lapse rates are calculated using a linear regression of the available data recorded between 700 and 3100 m (Figures 7e–7j).

[40] Because usage of a linear lapse rate ignores potential fine-scale atmospheric structure it is important to assess the impact of this simplification on both propagation times and acoustic focusing factors. We trace acoustic raypaths for both the original radiosonde profiles and the linear regression by conserving ray parameters (Figure 8b). Reassuringly, the corresponding propagation times and acoustic power ratios (calculated according to equation (15)) show very good agreement (compare pentagram and hexagram symbols in Figure 8d). We conclude that fine-scale structure has relatively minimal influence on these parameters and, conversely, that our atmospheric inversions are capable of reproducing important gross-scale features (i.e., the average lapse rate) of the atmosphere.

[41] Overall, the average effective sound speeds and lapse rates from the radiosonde data compare favorably with the infrasound-inferred effective sound speeds in Figures 9b and 9c. In particular, the Julian day 061 data and inversion results both show a strong negative lapse rate and a low average effective sound speed. A comparison of infrasound-inferred wind speeds and radiosonde NNW-projected winds at the heights of SUM and CON is also illustrative (Figure 11). For example, on Julian day 061 strongly opposing upper altitude winds are in evidence for both data, while on Julian day 066 the situation is reversed, with both the infrasound and radiosonde indicating a positive shear with altitude.

[42] Given the separation distance between infrasound sampling and radiosonde soundings it is important not to

overanalyze the data shown in Figure 11. Discrepancies between meteorological data and infrasound-inferred wind shear, most notably on days 063 and 065, may be plausibly attributed to structural differences at the two sampling locales, which are 230 km apart and in differing geographic settings. Another potentially important source of difference is the assumed linear adiabatic sound speed profile extracted from RT-130 temperature records.

[43] Future experiments will benefit from incorporation of adequate local ground-based meteorological observations. In addition, radiosondes should be launched from locales closer to the infrasound source and with greater temporal frequency in order to test the accuracy of the infrasonic probing. In general, we feel that an ‘infrasonic anemometer’ has potential to provide more accurate estimates of lower atmosphere averaged wind fields than a ground-based meteorological station, which samples only within the atmospheric boundary layer and is subject to localized site effects that are functions of topography and vegetation. In the case of continuous infrasound radiators, such as Villarrica, infrasound monitoring can provide continuous profiling of the atmosphere, which would be uneconomical with balloon launches.

5. Discussion

5.1. Comments on the Variability in Infrasound Strength Due to Atmospheric Focusing

[44] We have analyzed continuous volcano infrasound signal and shown that time-varying acoustic focusing is significant at a transmission distance of only 8 km. During periods of time in which wind appears to be opposed to the transmission direction the acoustic power at 8 km was diminished by as much as -8.5 dB, which is equivalent to dynamic acoustic power that is 14% of that expected in a homogeneous atmosphere. Converted to pressure amplitude this power diminution implies that excess pressure waveforms recorded at CON are as low as 38% of the expected level based upon pressures recorded at SUM.

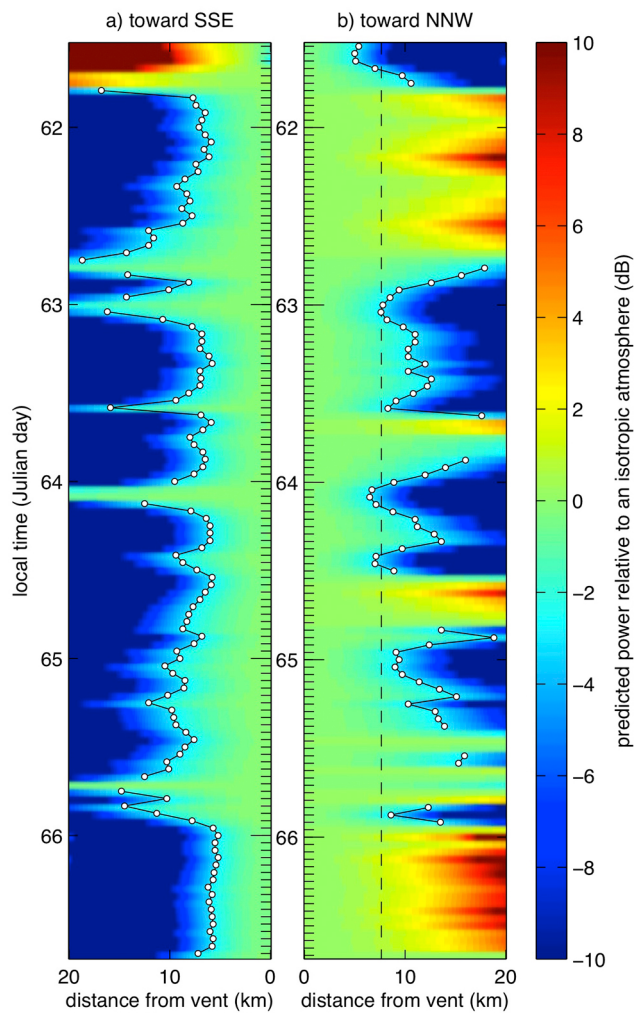


Figure 12. Modeled sound power ratios (in dB), relative to that for a homogeneous stationary atmosphere, for sound propagated to (a) the SSE and (b) the NNW (direction of CON from SUM). Acoustic power intensity is calculated for a uniform altitude that is 2001 m below Villarrica's summit. Red colors indicate predicted sound intensification and blue colors show sound diminution. White circles correspond to distances where modeled sound power is diminished by 3 dB.

[45] The period of weakest acoustic transmission toward CON (during Julian day 061) corresponds to propagation times between SUM and CON that were as great as 24.2 s (Figure 6) implying either exceptionally low adiabatic sound speeds (and temperatures) or strongly opposing winds. In fact, our field crew was unable to ascend Villarrica on Julian day 061 due to inclement weather in the form of strong winds and precipitation. On all subsequent days, when inferred winds were moderate and originating from the SSE, the weather on the mountain was settled. Conditions on these days allowed easy access to the summit where our team perceived winds even on the summit to be low to moderate.

[46] The greatest amount of acoustic power intensification, or signal increase relative to a stationary and homogeneous

atmosphere, occurred at about 3 A.M. on Julian day 066 and measured +1.9 dB corresponding to 1.5 times the energy amplification or 1.2 times the expected infrasonic pressure levels. Amplitude intensification appears to have occurred when higher altitude winds were blowing favorably toward the CON array and when there was a positive wind shear with height (refer to Figure 10d). Such structure appears to have focused NNW trending acoustic rays through downward refraction.

5.2. Prediction of Acoustic Audibility Patterns

[47] The variability of infrasound power focusing at 8 km is in of itself an important observation to have quantified. Previous work by *Fee and Garcés* [2007] analyzed volcano infrasound radiation out to ~ 12 km in the 'diffraction zone' and proposed that diurnal atmospheric variations were responsible for variable intensity in Kilauea volcano signals. This infrasound was alternately absent or pronounced, such as when a nighttime inversion formed in a 300-m boundary layer. Acoustic shadow zones are routinely identified at distances of many tens of kilometers, but at distances inboard of these shadow zones the relation between pressure amplitude decay and distance is often poorly quantified.

[48] Such uncertainty presents problems for volcano researchers who are interested in extrapolating both regional and global infrasound [Dabrowa *et al.*, 2011], as well as local infrasound recordings [Johnson *et al.*, 2004], to their associated eruption source intensity in order to model source processes and quantify acoustic energy flux [e.g., Johnson and Aster, 2005]. The continuous infrasound signal from Villarrica thus provides an ideal test bed to understand the limits where $1/r$ pressure distance fall-off is an appropriate approximation. Empirical observations of acoustic power densities also have implications for quantifying source strengths of other natural geophysical phenomena as well as human-produced sources.

[49] By extending our temporally varying inversion profiles to a more extensive 1-D space we may better understand infrasound focusing at distances inboard and beyond the 8 km range over which we have recorded signal in this study. Equation (15) may be applied to a range of distances to model intensification and diminution of signals for atmospheres with uniform effective sound speed lapse rates (Figure 12). Further, if we assume that winds are uniform in all directions from Villarrica's vent, then we may predict infrasound radiation in the opposite direction (e.g., to the SSE; Figure 12a), where effective sound speed is calculated according to equation (17).

[50] Sound power is enhanced when effective sound speed increases with altitude. This occurs, for example, when projected winds increase with height. For uniform wind fields this implies that sound power will be reduced for propagation in the opposite direction. During our study interval, the modeled high-altitude winds originated primarily from the SSE, which tended to refract sound back toward the ground. In contrast, the predicted acoustic power that would be recorded to the SSE is expected to fall off more quickly with distance (Figure 12). For our uniform lapse rate model the estimated acoustic power is 3 dB down at ~ 6 –8 km toward the SSE and 3 dB down at 10–12 km

toward the NNW. This modeled asymmetric power radiation can be easily tested in future field deployments.

6. Conclusion

[51] We have demonstrated that sound transmission parameters including travel time and acoustic power focusing can be robustly quantified using infrasound sensor arrays located proximally and at further distances from an intense, persistent volcano infrasound source. These time varying parameters provide constraints upon the atmospheric structure, including its average effective sound speed and its vertically averaged gradient. As such, persistent infrasound radiators, such as Volcan Villarrica, may be used to continuously monitor changing atmospheric conditions over time. Other similarly persistent volcanoes, such as Kilauea [Matoza *et al.*, 2010; Fee and Garcés, 2007; Marcillo and Johnson, 2010], and intermittently active volcanoes such as Tungurahua [Assink *et al.*, 2012] could also be used to quantify dynamic atmospheric structure.

[52] The inferred atmospheric structures inverted for in this initial study presume vertically varying profiles, where effective sound speeds change linearly with height and winds are confined to a horizontal plane. Future studies, in which a distributed network of infrasonic stations would be deployed, could be used to resolve multidimensional atmospheric heterogeneities. Potentially, infrasonic stations located at distributed azimuths and distances can be used to track the 4-D atmosphere. Incorporation of additional ground-based meteorological stations or radiosonde measurements would be vital for corroboration of model results.

[53] Probing the atmosphere with infrasound provides meteorological sampling that extends above the atmosphere-Earth boundary layer and avoids biasing that occurs during point-location measurements influenced by local site effects. These wind fields are relevant for modeling transport of air parcels and/or aerosols in the atmosphere. Such results should be of interest to volcanologists, who are interested in quantifying gas emissions and predicting dispersal of volcanic plumes.

Notation

Symbols used in the analyses are described in text and summarized in this table. A range of values is provided parenthetically for parameters relevant to this study. Annotation is listed in the order introduced in the text.

ΔT	Propagation time between SUM3 and CON (23.0–24.2 s)
r	Radial distance (m)
Ω	Solid angle (unitless)
θ	Apex angle of cone (degrees)
$c\rho$	Impedance (product of sound speed and density) ($\text{kg m}^{-2} \text{s}^{-1}$)
j	Station index (SUM or CON)
w_j	Cumulative energy density calculated at station j (J m^{-2})
p_j	Pressure recorded at station j (Pa)
p_{rms}	Root mean squared (RMS) pressure (Pa)
W_j	Cumulative acoustic energy at radial distance r_j (J)
t_0	Time window start at source samples

τ	Window duration (60,000 samples)
$p(\omega)$	Discrete Fourier transform of excess pressure (Pa/radians s^{-1})
ω_l and ω_h	Low and high angular frequency limits (radian s^{-1})
P_j	Band-limited power at station j (W)
P_R	Power ratio of CON relative to SUM1 (unitless)
$c(z)$	Altitude-dependent effective sound speed (310–355 m s^{-1})
$v(z)$	Adiabatic sound speed (320–345 m s^{-1})
$\vec{u}(z)$	Horizontal wind vector (m s^{-1})
r	Horizontal component of sound propagation unit vector between SUM and CON (\sim NNW) ($-0.38^x + 0.92^y$)
α	Lapse rate ($\text{m s}^{-1} \text{m}^{-1}$)
c_0, c_{CON}, c_{SUM}	Effective sound speed at raypath origin and at height of CON and SUM respectively (m s^{-1})
X, Z	Distances from SUM3 to CON1 (7654 m, 2001 m)
$i(z)$	Incidence angle measured from vertical at altitude z (degrees)
s_x	Ray parameter (horizontal slowness) (s m^{-1})
x, z	Radial distance to NNW of summit and vertical distance above the level of CON m
$t(x)$	Travel time to horizontal distance x (s)
$R(s_x)$	Residual calculated as a function of slowness (unitless)
$\varepsilon(z)$	Substitution for horizontal slowness and altitude-dependent effective sound speed (unitless)
$E(x)$	Normalized energy density as a function of horizontal distance for stratified medium (m^{-2})
$E_H(x)$	Normalized energy density for a homogeneous medium (m^{-2})
γR	Product of heat capacity ratio and ideal gas constant 402.8 ($\text{m}^2 \text{s}^2 \text{K}^{-1}$)
$T(z)$	Altitude-varying temperature (270–300 K)
$c_{opp}(z)$	Effective sound speed in opposing direction (m s^{-1})

[54] **Acknowledgments.** We thank R. Sanderson and W. McIntosh for their invaluable field assistance and acknowledge J. Bustamente, the Mountain Guides Association of Pucon, and the Chilean Forest Service (CONAF) for their cooperation. The presented data were collected and analyzed through financial support from NSF EaGER grant 1127696 and NSF CAREER grant 1151662. We appreciate three anonymous reviewers for their valuable input.

References

- Assink, J. D., R. Waxler, and D. Drob (2012), On the sensitivity of infrasonic traveltimes in the equatorial region to the atmospheric tides, *J. Geophys. Res.*, *117*, D01110, doi:10.1029/2011JD016107.
- Barrientos, S., F. Riquelme, N. Brachet, A. Kramer, and P. Campus (2009), Llaima and Villarrica Volcanoes in south-central Chile: An infrasound factory, paper presented at International Scientific Studies, Hofburg Congr. Cent., Vienna.
- Bass, H. E., and H. J. Bauer (1972), Atmospheric absorption of sound: Analytical expressions, *J. Acoust. Soc. Am.*, *52*(3B), 821–825, doi:10.1121/1.1913183.
- Bowman, J. R., G. E. Baker, and M. Bahavar (2005), Ambient infrasound noise, *Geophys. Res. Lett.*, *32*, L09803, doi:10.1029/2005GL022486.
- Dabrowa, A. L., D. N. Green, A. C. Rust, and J. C. Phillips (2011), A global study of volcanic infrasound characteristics and the potential for long-

- range monitoring, *Earth Planet. Sci. Lett.*, *310*, 369–379, doi:10.1016/j.epsl.2011.08.027.
- Dowling, A. P. (1998), Steady-state radiation from sources, in *Handbook of Acoustics*, edited by M. Crocker, pp. 99–117, John Wiley, New York.
- Drob, D. P., R. R. Meier, J. M. Picone, and M. M. Garcés (2010), Inversion of infrasound signals for passive atmospheric remote sensing, in *Infrasound Monitoring for Atmospheric Studies*, edited by A. Le Pichon, E. Blanc, and A. Hauchecorne, pp. 701–731, Springer, Dordrecht, Netherlands, doi:10.1007/978-1-4020-9508-5_24.
- Dziewonski, A. M., and J. H. Woodhouse (1987), Global images of the Earth's interior, *Science*, *236*, 37–48, doi:10.1126/science.236.4797.37.
- Fee, D., and M. Garcés (2007), Infrasonic tremor in the diffraction zone, *Geophys. Res. Lett.*, *34*, L16826, doi:10.1029/2007GL030616.
- Fee, D., M. Garcés, M. Patrick, B. Chouet, P. B. Dawson, and D. Swanson (2010), Infrasonic harmonic tremor and degassing bursts from Halema'ūma'ū Crater, Kilauea Volcano, Hawaii, *J. Geophys. Res.*, *115*, B11316, doi:10.1029/2010JB007642.
- Garcés, M. A., R. A. Hansen, and K. Lindquist (1998), Traveltimes for infrasonic waves propagating in a stratified atmosphere, *Geophys. J. Int.*, *135*(1), 255–263, doi:10.1046/j.1365-246X.1998.00618.x.
- Goto, A., and J. B. Johnson (2011), Monotonic infrasound and Helmholtz resonance at Volcan Villarrica (Chile), *Geophys. Res. Lett.*, *38*, L06301, doi:10.1029/2011GL046858.
- Haney, M. M. (2009), Infrasonic ambient noise interferometry from correlations of microbaroms, *Geophys. Res. Lett.*, *36*, L19808, doi:10.1029/2009GL040179.
- Johnson, J. B., and R. C. Aster (2005), Relative partitioning of acoustic and seismic energy during Strombolian eruptions, *J. Volcanol. Geotherm. Res.*, *148*, 334–354, doi:10.1016/j.jvolgeores.2005.05.002.
- Johnson, J. B., and M. Ripepe (2011), Volcano infrasound: A review, *J. Volcanol. Geotherm. Res.*, *206*, 61–69, doi:10.1016/j.jvolgeores.2011.06.006.
- Johnson, J. B., R. C. Aster, and P. R. Kyle (2004), Volcanic eruptions observed with infrasound, *Geophys. Res. Lett.*, *31*, L14604, doi:10.1029/2004GL020020.
- Lalande, J.-M., O. Sebe, M. Landes, P. Blanc-Benon, R. S. Matoza, A. Le Pichon, and E. Blanc (2012), Infrasound data inversion for atmospheric sounding, *Geophys. J. Int.*, *190*(1), 687–701, doi:10.1111/j.1365-246X.2012.05518.x.
- Lay, T., and T. Wallace (1995), *Modern Global Seismology*, 521 pp., Academic, San Diego, Calif.
- Le Pichon, A., E. Blanc, D. Drob, S. Lambotte, J. X. Dessa, M. Lardy, P. Bani, and S. Vergnolle (2005), Infrasound monitoring of volcanoes to probe high-altitude winds, *J. Geophys. Res.*, *110*, D13106, doi:10.1029/2004JD005587.
- Marcillo, O., and J. B. Johnson (2010), Tracking near-surface atmospheric conditions using an infrasound network, *J. Acoust. Soc. Am. Lett.*, *128*(1), EL14–EL19, doi:10.1121/1.3442725.
- Marcillo, O., J. B. Johnson, and D. Hart (2012), Implementation, characterization, and evaluation of an inexpensive low-power low-noise infrasound sensor based on a micro-machined differential pressure transducer and a mechanical filter, *J. Atmos. Oceanic Technol.*, doi:10.1175/JTECH-D-11-00101.1, in press.
- Matoza, R. S., D. Fee, and M. A. Garcés (2010), Infrasonic tremor wavefield of the Pu'u 'Ō'ō crater complex and lava tube system, Hawaii in April 2007, *J. Geophys. Res.*, *115*, B12312, doi:10.1029/2009JB007192.
- Munk, W. H., and A. M. G. Forbes (1989), Global ocean warming: An acoustic measure?, *J. Phys. Oceanogr.*, *19*, 1765–1778, doi:10.1175/1520-0485(1989)019<1765:GOWAAM>2.0.CO;2.
- Ripepe, M., E. Marchetti, C. Bonadonna, A. J. L. Harris, L. Pioli, and G. Uliveri (2010), Monochromatic infrasonic tremor driven by persistent degassing and convection at Villarrica Volcano, Chile, *Geophys. Res. Lett.*, *37*, L15303, doi:10.1029/2010GL043516.
- Slotnick, M. M. (1959), *Lessons in Seismic Computing*, 268 pp., Soc. of Explor. Geophys., Tulsa, Okla.
- Stull, R. B. (2000), *Meteorology for Scientists and Engineers*, 2nd ed., 502 pp., Brooks/Cole, Pacific Grove, Calif.
- Vavryčuk, V. (1994), Energy balance of simple elastodynamic sources, *Pure Appl. Geophys.*, *143*(4), 563–586, doi:10.1007/BF00879498.
- Wilson, D. K., A. Ziemann, V. E. Ostashev, and A. G. Voronovich (2001), An overview of acoustic travel-time tomography in the atmosphere and potential applications, *Acta Acustica*, *87*, 721–730.